

# Perfusion alters stiffness of deep gray matter

Stefan Hetzer<sup>1,2</sup>, Patric Birr<sup>3</sup>, Andreas Fehlner<sup>3</sup>, Sebastian Hirsch<sup>4</sup>, Florian Dittmann<sup>3</sup>, Eric Barnhill<sup>3</sup>, Jürgen Braun<sup>4</sup> and Ingolf Sack<sup>3</sup>

## Abstract

Viscoelastic properties of the brain reflect tissue architecture at multiple length scales. However, little is known about the relation between vital tissue functions, such as perfusion, and the macroscopic mechanical properties of cerebral tissue. In this study, arterial spin labelling is paired with magnetic resonance elastography to investigate the relationship between tissue stiffness and cerebral blood flow (CBF) in the in vivo human brain. The viscoelastic modulus,  $|G^*|$ , and CBF were studied in deep gray matter (DGM) of 14 healthy male volunteers in the following sub-regions: putamen, nucleus accumbens, hippocampus, thalamus, globus pallidus, and amygdala. CBF was further normalized by vessel area data to obtain the flux rate  $q$  which is proportional to the perfusion pressure gradient. The striatum (represented by putamen and nucleus accumbens) was distinct from the other DGM regions by displaying markedly higher stiffness and perfusion values.  $q$  was a predictive marker for DGM stiffness as analyzed by linear regression  $|G^*| = q \cdot (4.2 \pm 0.6) \text{ kPa} \cdot \text{s} + (0.80 \pm 0.06) \text{ kPa}$  ( $R^2 = 0.92$ ,  $P = 0.006$ ). These results suggest a high sensitivity of MRE in DGM to perfusion pressure. The distinct mechano-vascular properties of striatum tissue, as compared to the rest of DGM, may reflect elevated perfusion pressure, which could explain the well-known susceptibility of the putamen to hemorrhages.

## Keywords

Deep gray matter, perfusion, elasticity, ASL, MRE, mechanical properties

Received 26 August 2016; Revised 15 December 2016; Accepted 3 January 2017

## Introduction

Brain function and neural health are related to the biophysical properties of cerebral tissues at a large number of scales. Biophysical properties include viscoelastic constants and fluid flow properties such as tissue perfusion—two properties which in the brain possibly influence each other.

Biological tissue is composed of multiple phases, one of which being the blood which flows through dispersed micro vessels embedded in solid tissue fractions.<sup>1–3</sup> Even though the total brain volume occupied by blood vessels is less than 3%, the average distance between a neuron and a microvessel in brain gray matter (GM) is about 20  $\mu\text{m}$ .<sup>4</sup> Hence, viscoelastic parameters of in vivo brain tissue reflect effective medium properties which integrate both solid and vascular properties as well as the interactions thereof.<sup>5–11</sup>

Rheological models based on poroelasticity or micro-vascular flow can predict the macroscopic mechanical response of multiphase soft tissues such as the brain by taking into account altered fluid properties. Fluid transport in the brain refers to different phenomena measured in different units and at different

<sup>1</sup>Berlin Center for Advanced Neuroimaging, Charité – Universitätsmedizin Berlin, Berlin, Germany

<sup>2</sup>Bernstein Center for Computational Neuroscience, Berlin, Germany

<sup>3</sup>Department of Radiology, Charité – Universitätsmedizin Berlin, Berlin, Germany

<sup>4</sup>Institute of Medical Informatics, Charité – Universitätsmedizin Berlin, Berlin, Germany

### Corresponding author:

Stefan Hetzer, Berlin Center for Advanced Neuroimaging, Charité – Universitätsmedizin Berlin, Charitéplatz 1, Berlin 10117, Germany.  
 Email: [Stefan.Hetzer@charite.de](mailto:Stefan.Hetzer@charite.de)

temporal-spatial scales including water diffusion in white matter (WM) ( $\sim 0.8 \times 10^{-3} \text{ mm}^2/\text{s}$ ),<sup>12</sup> cerebrospinal fluid (CSF) flow through the aqueduct ( $\sim 4.3 \text{ ml}/\text{min}$ ),<sup>13</sup> cerebral arterial blood flow ( $\sim 650 \text{ ml}/\text{min}$ )<sup>14</sup> and tissue perfusion which is normally quantified by the parameter of cerebral blood flow (CBF) in units of volume/min normalized for 100 g tissue. The scale of perfusion relates to the topology and geometry of micro vessels<sup>15</sup> which have been postulated to significantly influence the global shear modulus of soft biological tissues.<sup>3</sup> As such, CBF which ranges from 40 and 100 ml/min/100 g in human gray matter<sup>16</sup> potentially influences the macroscopic viscoelastic response of brain tissue in particular with regard to ex vivo methods<sup>17</sup> and in vivo magnetic resonance elastography (MRE).<sup>18</sup>

Despite these intriguing relationships, CBF and viscoelasticity of the human brain have not yet been analyzed together. Here we present the first investigation pairing high-resolution, spatially resolved maps of both CBF and viscoelasticity. Both maps can be acquired *in vivo* using MRI without contrast agents. Arterial spin labelling (ASL)<sup>19</sup> is used for acquiring CBF maps. Viscoelastic maps are created by propagating mechanical waves into the brain and analyzing the resulting wave patterns with the method of MRE,<sup>20</sup> which has been successfully applied in studies of different neurological disorders, such as multiple sclerosis,<sup>21</sup> amyotrophic lateral sclerosis,<sup>22</sup> dementia,<sup>23</sup> as well as stroke<sup>24,25</sup> and brain tumors.<sup>26</sup>

ASL and MRE are not equally effective for imaging all brain tissues: MRE faces challenges imaging cerebral gray matter (GM) due to partial-volume effects near brain external boundaries. Quantifying white matter (WM) perfusion with ASL remains challenging due to approximately three times reduced perfusion rate than in GM<sup>27</sup> and roughly two times longer arterial transit times (ATT),<sup>28</sup> which greatly reduce signal-to-noise ratio (SNR). Consequently, this study focused on the relationship between CBF and  $|G^*|$  in deep gray matter (DGM) regions containing sufficient volume to ensure statistical robustness. The present study correlated the results obtained by ASL and MRE, aiming for a synergetic biophysical-based quantification of tissue-structural differences among DGM tissues.

## Material and methods

Fourteen healthy male subjects were investigated in a 3T MRI scanner (Siemens Magnetom Trio, Erlangen, Germany) after written informed consent was obtained. The study was approved by the Ethics Committees of the Charité – Universitätsmedizin Berlin in conformity with the Declaration of Helsinki. A Magnetization

Prepared Rapid Acquisition Gradient Echo (MPRAGE) scan with 1 mm isotropic resolution was acquired for T1-weighted anatomical reference prior to MRE and ASL.

## Multifrequency MRE

MRE was performed utilizing a head cradle actuator connected to a piezo-electrical vibration generator as detailed by Guo et al.<sup>34</sup> Three vibration frequencies of 30, 40 and 50 Hz were consecutively applied. Image acquisition was performed in a 12-channel radio-frequency (RF) coil using a single-shot spin-echo echo planar imaging (EPI) sequence sensitized to motion by a single-cycle bipolar motion encoding gradient (MEG).<sup>6</sup> Full wave field data were acquired in 40 contiguous transversal slices of 2 mm isotropic resolution. Further imaging parameters: echo time  $TE = 82 \text{ ms}$ , repetition time  $TR = 8.49 \text{ s}$ , matrix size  $88 \times 100$ , 20 ms single-cycle flow compensated MEG of 35 mT/m amplitude, eight acquisitions over a wave cycle. Total scan time for MRE was approximately 10 min.

MRE images were processed by a multi-frequency MRE processing pipeline to generate high-resolution maps of viscoelastic properties as outlined by Streitberger et al.<sup>35</sup> In short, high-resolution elastograms were obtained after the following steps: a) derivative-based unwrapping<sup>36</sup> after 2D Gaussian denoising of complex MRI data with 5 pixel edge size and  $\sigma = 0.65$ . As result, two images of in-plane strain components are obtained for each field component, i.e.  $\partial u_j / \partial x_k$  with  $j \in \{1, 2, 3\}$  and  $k \in \{1, 2\}$  according to Streitberger et al.<sup>35</sup> (b) Temporal Fourier transformation to generate six complex-valued wave derivative images for each frequency. (c) Second noise suppression by a 2D Butterworth lowpass filter with a threshold of  $100 \text{ m}^{-1}$ . Note that wave denoising was applied before each spatial derivative operation since numerical derivatives enhance noise.<sup>36</sup> (d) Multi-frequency dual elasto-visco inversion (MDEV). MDEV inversion provides high-resolution maps of the complex-valued shear modulus  $G^*$ ,<sup>37</sup> the magnitude of which  $|G^*|$  is a measure of tissue stiffness whereas the phase angle  $\varphi$  is a measure of tissue viscosity.<sup>34,38,39</sup>

## Arterial spin labelling

A pseudo-continuous arterial spin-labelling (pCASL) sequence<sup>29</sup> and a 32-channel RF head coil were used for perfusion imaging with 2.5 mm isotropic voxel resolution. A total of 120 volumes (60 controls and 60 labels) were acquired with a repetition time of 4.7 s resulting in an acquisition time of 10 min. The label duration of  $\tau = 1.5 \text{ s}$  was followed by a post-labeling delay (PLD) of  $w = 1.2 \text{ s}$  and a gradient echo EPI

readout covering the whole brain with 32 ascending transversal slices (0.25 mm gap), matrix size  $72 \times 80$ , echo time  $TE = 18$  ms, and echo spacing 0.47 ms.

In order to optimize SNR and ASL scan time, we chose a label duration and PLD within the range of parameters optimized to avoid intravascular artifacts in healthy-subject ASL studies similar to ours with voxel volumes roughly six times smaller<sup>30</sup> than recommended for conventional clinical studies.<sup>16</sup> It is worth noting that the *effective* PLD in our study is around  $(2.0 \pm 0.7)$  s in DGM resulting from the 2-s long high-resolution EPI readout with slices acquired in ascending order. The PLD should be just longer than the longest arterial transit time present in the brain varying between 500 ms and 1500 ms for gray matter of healthy subjects depending on the tissue location.<sup>16</sup> Properly selected longer PLDs should be used for the applications in patient populations with increased transit times.<sup>16</sup>

ASLtbx<sup>31</sup> was used without smoothing for quantifying CBF in units of ml/100 g/min from the pCASL signal difference  $\Delta M$  of control and label images using the formula<sup>16,32</sup>

$$CBF = \frac{60 \cdot 100 \lambda \Delta M e^{w/T_1}}{2 \alpha T_1 M_0 (1 - e^{-\tau/T_1})} \quad (1)$$

For the present work, the following parameters were used:  $T_1 = 1664$  ms for the longitudinal relaxation time of the blood at 3 T,  $\alpha = 0.85$  for the labeling efficiency.  $M_0$  is the equilibrium magnetization of the local tissue element in the control image. The brain–blood water partition coefficient  $\lambda = 0.9$  ml/g calibrates CBF to units of ml/mg assuming instantaneous exchange of labeled water protons between blood and tissue—an assumption which has been discussed in the literature since long.<sup>61</sup> Although typically  $\lambda$  is used with the dimension of ml/g, it can be given as dimensionless ratio  $\lambda'$  in g/g and it changes with the type of tissue (from 0.96 g/g whole brain to 1.04 g/g in gray matter.<sup>62</sup> We henceforth considered the cerebral blood flow in the dimension 1/s which represents the rate of transport of unit blood volume, i.e.

$$CBF' = \frac{CBF \cdot \lambda}{60 \cdot 100 \cdot \lambda'} \quad (2)$$

### Flux rate and perfusion pressure gradient

To account for the local perfusion pressure gradient, CBF values were normalized to the mean area of the transport pipelines  $A$  obtained from non-invasive vessel size imaging employing hypercapnia in healthy subjects.<sup>33</sup> As a result, the flux rate  $q$  through the capillary

bed in 1/s was obtained

$$q = \frac{CBF'}{A} \text{ with } A = N \cdot \pi r^2 \quad (3)$$

$A$  relates to the density  $N$  of capillaries (number per  $\text{mm}^2$ ) and mean radii  $r$  of the micro vessels as measured by vessel size imaging.<sup>33</sup>  $q$  is the specific transport velocity of blood through the area of the vessels, i.e. discharge per unit area. Since we accounted above for  $CBF'$  as flow of unit volume and  $A$  as normalized vessel area,  $q$  is the flux rate of blood through the normalized vessel area. This model resembles fluid flow through porous media. In poroelasticity theory, Darcy's law relates the fluid flux rate through a porous material with the pressure gradient  $\nabla p$  and the hydraulic conductivity by

$$\vec{q} = -\kappa \nabla p \quad (4)$$

We adopted this relationship by taking  $\kappa$  as the hydraulic conductivity within the capillary system of DGM and  $\nabla p$  as the corresponding vascular pressure gradient, which we identified as the gradient of the local perfusion pressure. Consequently,  $\kappa$  denotes the ease at which blood travels through a vasculature and which depends on blood viscosity as well as geometrical parameters such as the tortuosity of the pipelines.

Opposed to equation (4), the flux rate  $q$  given in equation (3) and used throughout the paper has a scalar value since we did not consider any directionality of  $A$  which would require analysis of the components of  $q$  along the normals of the area through which the blood traverses. In further distinction to Darcy's law, we only considered vascular spaces in  $A$  and did not account for the total tissue area. Hence, the CBF signal normalized by the vessel size  $A$  gave us a measure of vascular flux rate  $q$  of blood driven by the magnitude perfusion pressure gradient

$$\frac{CBF'}{A} \propto |\nabla p| \quad (5)$$

As example, a CBF of 45 ml/min/100 g as measured in the putamen in our study, a mean vessel radius of  $6.2 \mu\text{m}$ ,<sup>33</sup>  $\lambda' = 0.96$  g/g, and an approximated vessel density<sup>52,63</sup> of  $N = 400/\text{mm}^2$  gave  $q = 0.17 \text{ s}^{-1}$ .

### Post-processing of CBF- and MRE-maps

All images were post-processed using Matlab (MathWorks, Natick, MA, USA), SPM12 (Wellcome Trust Centre for Neuroimaging, London, UK) and the FMRIB Software Library (FSL v. 5, Oxford Centre for Functional MRI of the Brain, Oxford, UK) for correcting motion and field distortion artifacts.

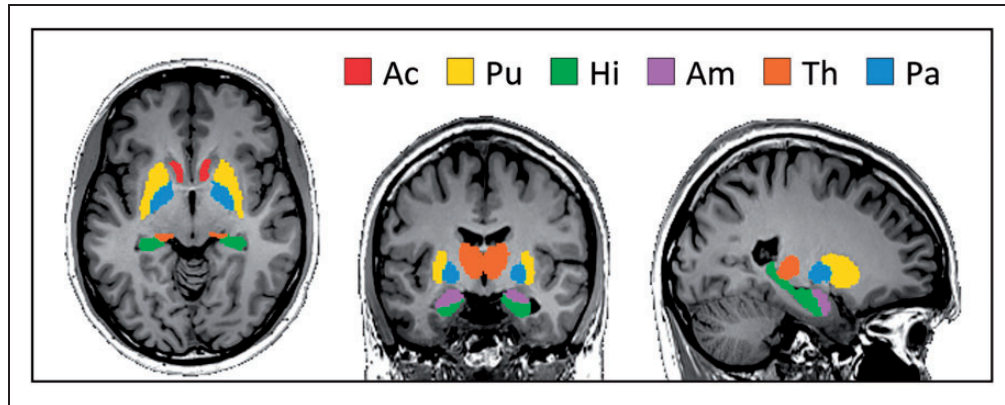


**Figure 1.** Analyzed deep-gray matter regions of the Neuromorphometrics Atlas in MNI space. Red: Nucleus Accumbens (Ac), yellow: Putamen (Pu), green: Hippocampus (Hi), pink: Amygdala (Am), orange: Thalamus (Th), blue: Globus Pallidus (Pa).

Before parameter quantification, subject motion and geometric distortions induced by  $B_0$  inhomogeneities were corrected with a pipeline increasing the spatial precision for both magnitude-based contrasts (e.g. ASL) and phase-based contrasts (e.g. MRE).<sup>40</sup> In order to allow for inter-subject statistics, all individual CBF and MRE maps were normalized to fit the dimensions of the Neuromorphometrics atlas of brain regions (neuromorphometrics.com) delivered by SPM12 in the anatomical standard space defined by the Montreal Neurological Institute brain template (MNI)<sup>41</sup> by employing the combined spatial normalization and segmentation algorithm included in SPM12. For morphing the individual maps to the template space, the default of 1176 parameters was employed by the SPM routine for optimizing the non-linear 3D deformation field based on linear combinations of discrete cosine transform basis functions. The tissue probability map of CSF was used to eliminate voxels in the vicinity (within a radius of 2 mm) of CSF in order to avoid partial volume effects<sup>42</sup> influencing the analysis. The combination of co-registration and removal of CSF boundary pixels resulted in small numbers of remaining voxels in some DGM tissues which threatened statistical robustness. We therefore analyzed only those regions in which more than 30% of all pixels were preserved after the removal of boundary pixels. Overall six regions fulfilled this criterion (see Figure 1): putamen (Pu), nucleus accumbens (Ac), hippocampus (Hi), thalamus (Th), globus pallidus (Pa) and amygdala (Am). Average  $|G^*|$ ,  $\varphi$ , and CBF values of all subjects were calculated in each region separately.

A two-tailed  $t$ -test with a 5% significance level was applied to the regional comparisons of  $|G^*|$ ,  $\varphi$  and CBF. The Holm-Bonferroni method<sup>43</sup> was used to detect DGM areas that can be significantly separated. The correlation between parameters was tested by Pearson's pairwise linear correlation coefficient.

All coefficients of determination  $R^2$  of linear regressions were adjusted for the number of observations and the number of variables. Cluster analysis for the  $|G^*|$ -CBF space was performed by a post-hoc silhouette analysis.<sup>44</sup> Clusters and silhouettes were generated in Matlab using the `kmeans` and `silhouette` functions.

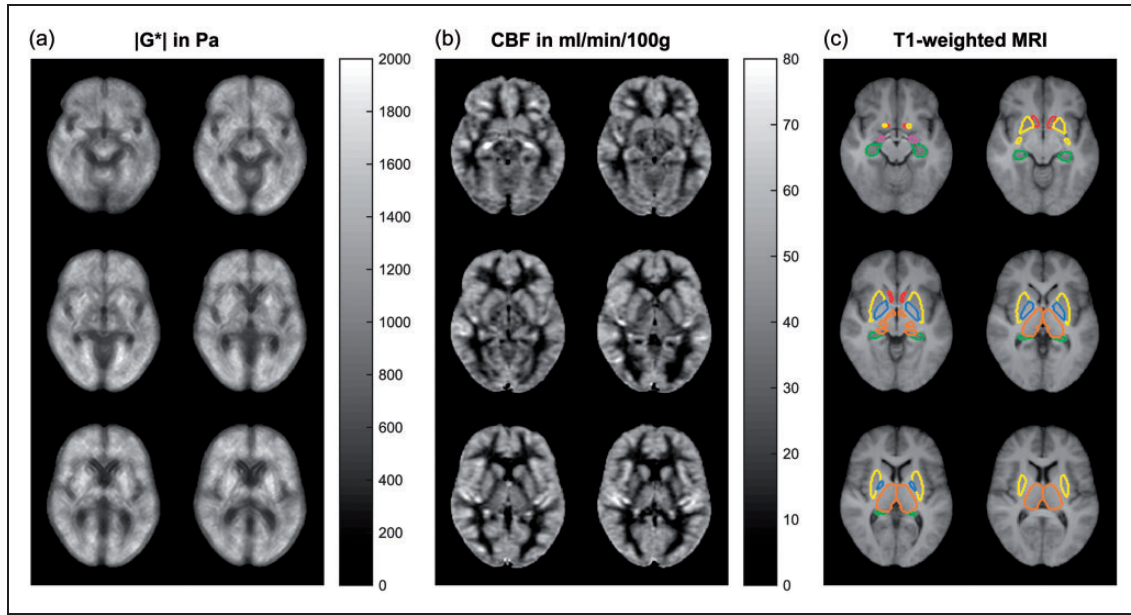
## Results

Figure 2 shows three group-mean  $|G^*|$ - and CBF maps and corresponding T1-weighted anatomical scans with the six analyzed DGM regions corresponding to the regions shown in Figure 1 and according to the Neuromorphometrics Atlas. Group mean  $|G^*|$  and CBF values are listed in Table 1. Figure 3 additionally shows values independently obtained from the right and left hemisphere indicating the consistency of values with respect to inter-hemispherical symmetry. Therefore, the analysis proceeded using the values averaged over both contra lateral regions.

By group analysis, the striatum region (represented by Pu and Ac) displayed higher  $|G^*|$  and CBF values than the rest of DGM ( $|G^*| = 1.49 \pm 0.16$  vs.  $1.10 \pm 0.14$  kPa,  $P = 8.7 \times 10^{-11}$ ; CBF =  $47 \pm 10$  vs.  $37 \pm 7$  ml/100g/min,  $P = 3.0 \times 10^{-6}$ ). The significance of discriminating between DGM regions based on MRE and ASL is indicated by the plot of  $P$ -values in Figure 4. Interestingly, MRE separates putamen (Pu) from all other regions while CBF exhibits a larger overlap as demonstrated by silhouette plots for  $|G^*|$  and CBF by region shown in Figure 5(a). There it can be seen that a two-cluster partition of striatum tissue (Pu, Ac) versus the rest of DGM (Pa, Th, Am, Hi) produces the highest separation values quantified as the highest mean silhouette value for the chosen partition (0.63 mean silhouette distance).

While the group-analysis based on pooled data showed no significant linear correlation between  $|G^*|$





**Figure 2.** Six slices of the three-dimensional  $|G^*|$  map (a) and CBF map (b) averaged over 14 volunteers and corresponding T1-weighted anatomical scans with the six analyzed DGM regions (c). Note that apparently high stiffness values in putamen (yellow) are associated with relatively high CBF values. Color codes correspond to Figure 1.

**Table 1.** Characteristic values for the analyzed deep gray matter regions.

	Putamen	Nucleus accumbens	Hippocampus	Thalamus	Globus pallidus	Amygdala
$ G^* $ in kPa	$1.58 \pm 0.24$	$1.41 \pm 0.11$	$1.0 \pm 0.11$	$1.14 \pm 0.17$	$1.19 \pm 0.27$	$1.07 \pm 0.13$
$\varphi$ in rad	$0.82 \pm 0.06$	$0.61 \pm 0.14$	$0.64 \pm 0.08$	$0.66 \pm 0.11$	$0.74 \pm 0.09$	$0.74 \pm 0.13$
CBF in ml/min/100 g	$45 \pm 10$	$50 \pm 10$	$40 \pm 8$	$36 \pm 7$	$33 \pm 7$	$38 \pm 10$
$r$ in mm	$6.2 \pm 0.7$	n/a	$11.3 \pm 2.1$	$8.8 \pm 1.6$	$6.7 \pm 1.0$	$11.4 \pm 2.5$
$q$ in $s^{-1}$	$0.17 \pm 0.03$	n/a	$0.04 \pm 0.01$	$0.07 \pm 0.01$	$0.10 \pm 0.02$	$0.04 \pm 0.01$

Note: Shear-modulus magnitude  $|G^*|$ , shear-modulus phase angle  $\varphi$ , cerebral blood flow (CBF), vessel radius  $r$  from literature<sup>33</sup> and the corresponding flux rate  $q$  in deep gray matter regions. Tolerance values reflect the inter-subject variability.

and CBF ( $R^2=0.28$ ,  $P=0.16$ ), the non-striatal cluster showed a strong inverse correlation ( $R^2=0.93$ ,  $P=0.02$ ). This linear decrease of  $|G^*|$  with increasing CBF is well demonstrated in Figure 6(a) by the Hi, Th, Pa and Am regions. In this  $|G^*|$ -CBF space, the striatum regions appear well separated from the rest of DGM. Notably, the clustering of two distinct regions is not perceivable on either of the two parameters' axes alone. No correlation between phase angle  $\varphi$  and CBF was observed ( $R^2=0.04$ ,  $P=0.71$  for pooled data;  $R^2=0.02$ ,  $P=0.44$  for non-striatal DGM regions).

To further analyze the origin of the two clusters in Figure 6(a) which separate the striatum from the rest of DGM, we derived the flux rate  $q$ , that is CBF normalized to the vessel size area  $A$  (see equation (3)) based on values reported in the literature.<sup>33</sup> Figure 6(b) shows, when normalizing CBF by  $A$ , the previously observed inverse correlation within non-striatal DGM regions

changes to a positive correlation between  $|G^*|$  and  $q$ , now covering all DGM regions for which  $A$  values could be calculated, including the putamen. Linear regression showed that  $|G^*|$  in DGM is strongly correlated to flux rate ( $R^2=0.922$ ) resulting in  $|G^*| = (0.80 \pm 0.06) \text{ kPa} + q \cdot (4.2 \pm 0.6) \text{ kPa}\cdot\text{s}$ . While the offset ( $P=0.0007$ ) has the physical unit of elasticity, the slope ( $P=0.0061$ ) of this linear equation has the physical unit of viscosity. No significant correlation between phase angle  $\varphi$  and  $q$  was observed ( $R^2=0.52$ ,  $P=0.11$ ). Table 1 summarizes regional MRE and ASL values measured in this study as well as vessel size data from the literature and derived flux rates  $q$ .

## Discussion

Effective-medium physical properties of biological tissues are becoming increasingly relevant for a

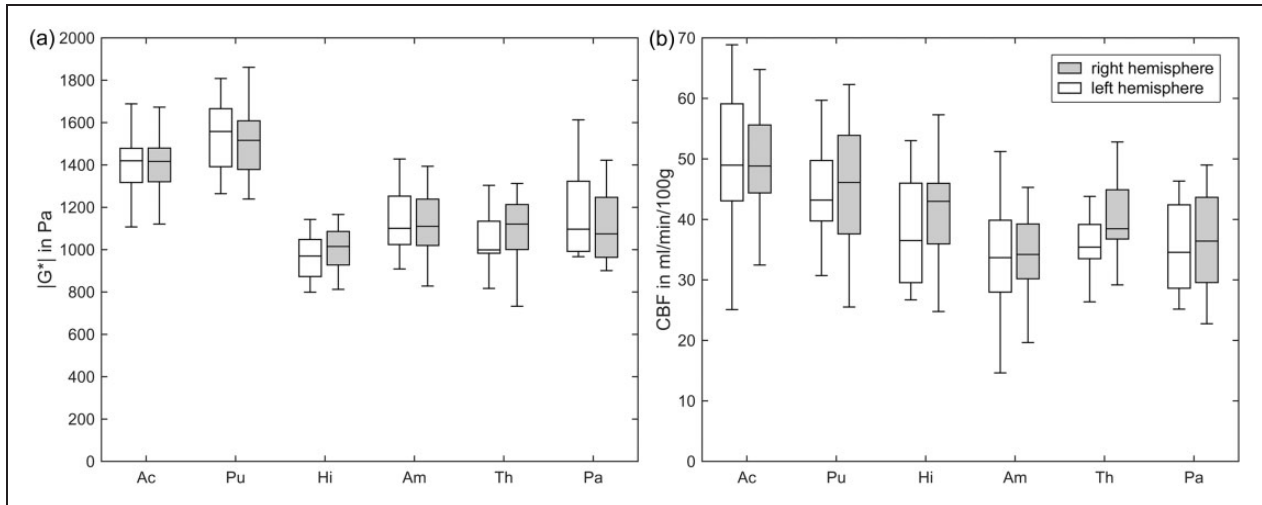


**Figure 3.** Stiffness  $|G^*|$  (a) and cerebral blood flow CBF (b) obtained by MRE and ASL in six DGM regions (sorted by average CBF value) analyzed in both hemispheres, indicating the consistency of values with respect to inter-hemispherical symmetry: no significant differences were observed between the hemispheres in all regions. Note high stiffness and perfusion values of the striatal DGM areas (Pu and Ac).

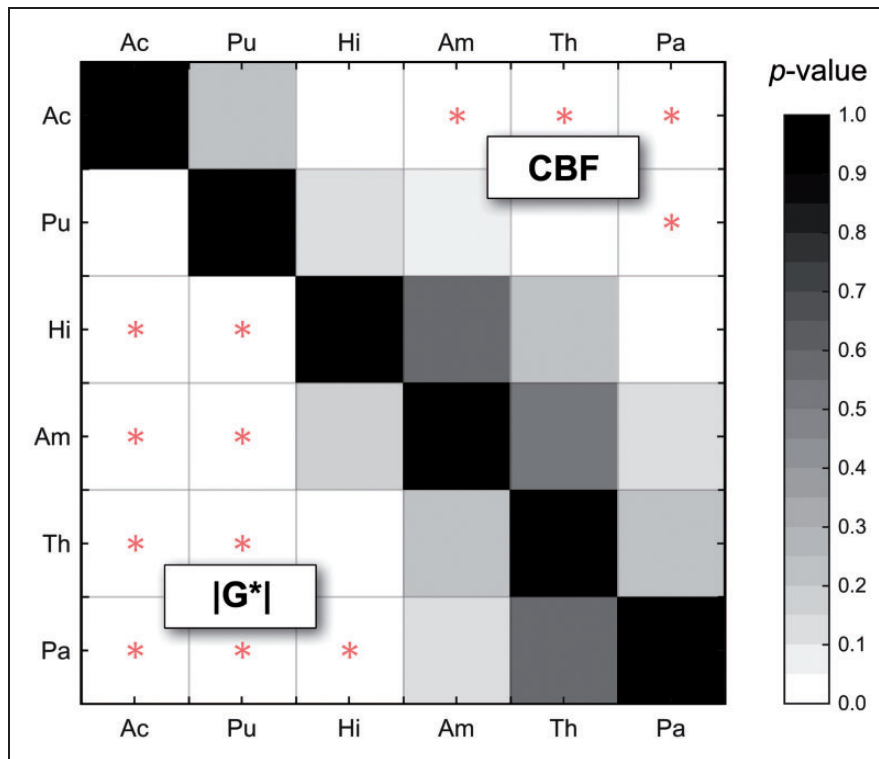


**Figure 4.** *P*-values based on paired Student’s *t*-tests for discriminating regions by  $|G^*|$  and CBF with MRE below and ASL above the matrix diagonal. In contrast to ASL, putamen (Pu) can be significantly separated from all other regions by MRE. Significant values after Holm-Bonferroni correction for multiple tests are marked by a red star.

quantitative clinical diagnosis based on medical imaging. In the brain, tissue perfusion and viscoelastic parameters have been shown to be highly sensitive to physiological effects and disease.<sup>45,46</sup> Our study shows

that perfusion alters the effective medium properties in the brain similar to recent findings in abdominal organs after water intake.<sup>47</sup> Dittmann et al. reported an increase of stiffness of the liver with increased blood

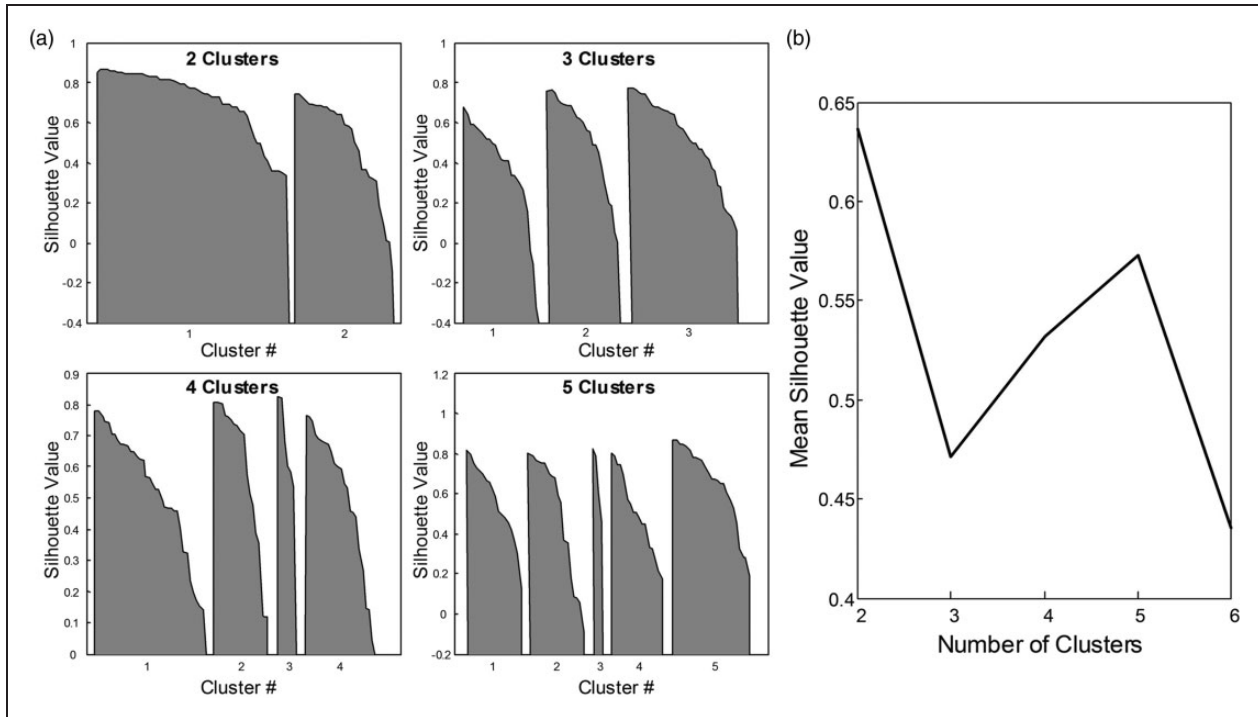


**Figure 5.** K-means silhouette analysis for  $|G^*|$ -CBF data. In panel (a), silhouette values (distance of each value in a cluster from all other clusters) are shown for choices of 2, 3, 4, and 5 partitions, respectively. The mean silhouette value for a choice of partition is commonly used to identify best fit of partition choice. Panel (b) shows that a partitioning of the data into two clusters produces the best separation of the  $|G^*|$ -CBF data as indicated by the highest mean silhouette value.

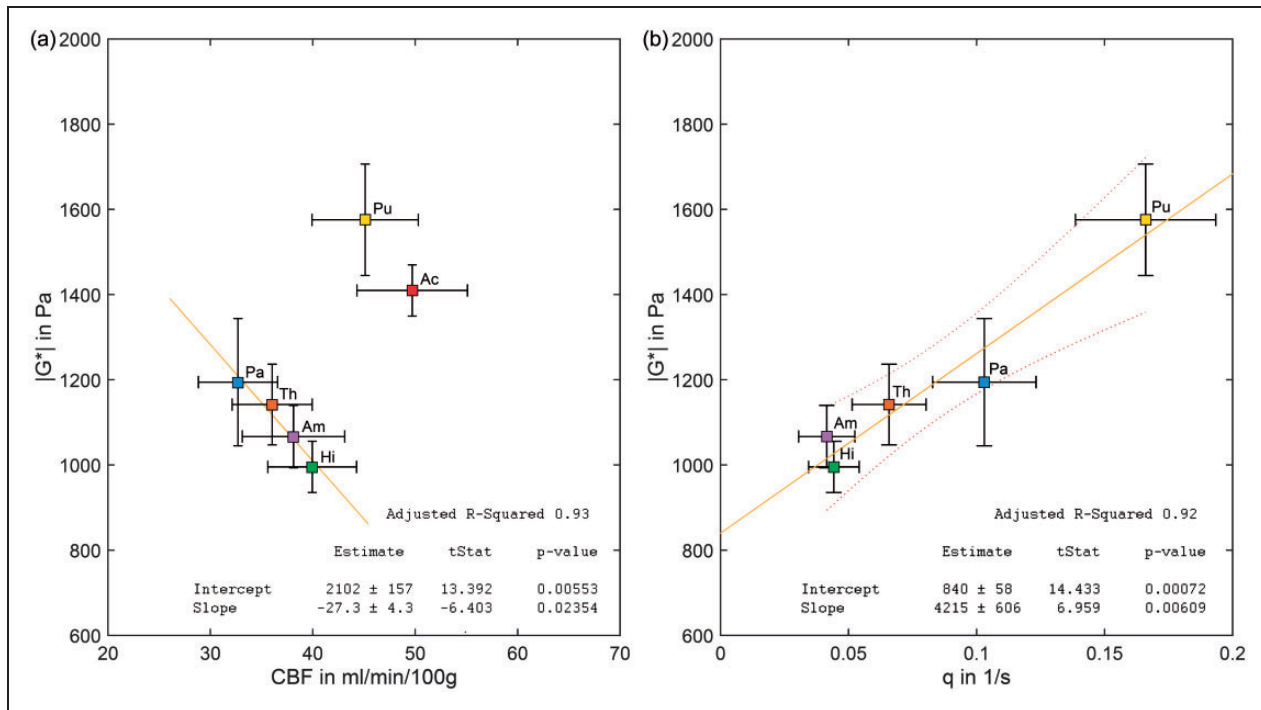


**Figure 6.** In vivo DGM of the human brain characterized by MRE and ASL. (a) The cluster of non-striatal DGM (Pa, Th, Am, Hi) reveals an inverse correlation between tissue stiffness ( $|G^*|$ ) and perfusion (CBF) in these regions. (b) When normalizing CBF by the mean cross-sectional vessel area (according to the five  $r$ -values given in Table 1), stiffness of all DGM areas including the putamen can be predicted from the flux rate  $q$  based on a linear regression model. Error bars reflect the standard error of the mean.

volume after water ingestion while stiffness reduced with increasing blood volume in the pancreas and spleen.<sup>47</sup> The authors discussed the opposite behavior of pancreas/spleen tissue versus liver based on the increased solid-to-fluid fraction in compliant tissue such as pancreas/spleen as opposed to the encapsulated liver which yields an increased perfusion pressure after water intake. This demonstrates the intricate relationship between blood perfusion and effective stiffness of in vivo tissue that may also play a role in DGM: Scenario 1 in our study is reflected by the inverse correlation of  $|G^*|$  with CBF suggesting the softening of tissue at higher fluid volume fractions (Figure 6(a)). Scenario 2 is reflected by the positive correlation of  $|G^*|$  and  $q$ , which takes into account that CBF is transmitted through different mean vessel areas  $A$  (Figure 6(b)). The difference between the two could be related to the intravascular pressure which is higher in smaller vessels or in vessels confined by non-compliant tissue.

The distinction between striatum and the other analyzed DGM regions within the  $|G^*|$ -CBF space suggests a distinct microstructure of the striatum. The medium-spiny neurons which make up 95% of the neuronal population of the striatum<sup>48</sup> are supplied by blood through a tight meshwork of capillaries with, on average, smaller mean vessel sizes than other DGM regions. It has been considered that this anatomical peculiarity constitutes a reason for the high prevalence of putaminal hemorrhages, that account for half of the brain hemorrhage cases.<sup>49,50</sup> The steepest pressure gradient is located in the capillary bed that offers the largest hemodynamic resistance to the cortical blood supply<sup>51</sup> and is thus most vulnerable to vascular rupture, e.g. in hypertension.<sup>49</sup> Our data demonstrate the feasibility of using MRE in DGM as an imaging marker for characterizing tissue with elevated vascular pressure. Pressure-related tissue parameters seem to be better addressed by MRE which measures modulus values in kPa than by ASL which needs further information such as vessel size and vessel density. Specifically, the mean vessel density is difficult to resolve locally by MRI as suggested by the large variety of data in the literature. For this reason, we used an averaged mean vessel density of  $N = 400/\text{mm}^2$  since no significant differences were found in  $N$  among DGM regions.<sup>52</sup>

As a limitation of our study, details in cortical gray matter were not resolved by MRE, since in MRE, cortical GM is considered prone to artifacts due to abundant tissue boundaries and has thus been excluded from many studies.<sup>34,42,53,54</sup>

A further limitation is that we report only ground truth values measured in the autoregulatory regime in healthy volunteers. This means that the hydraulic conductivity  $\kappa$  (or vascular resistance) in equation (4) is highly regulated in order to maintain a constant

blood flow despite variation in  $\nabla p$ . Our study cannot disentangle both variables in  $\kappa \nabla p$  from the measured flux rate. The observed regional variation of  $q$  reflects differences in  $\kappa$  and/or  $\nabla p$  within the limits of autoregulation. Exceeding the autoregulatory regime, the range of variation in  $q$  becomes larger causing a larger variation in  $|G^*|$  which, however, remains to be determined experimentally. Therefore, manipulations that alter CBF in volunteers or by investigating the  $|G^*|$ -CBF relationship in disease state, especially stroke, would be highly interesting.

Furthermore, we expected  $\varphi$ , as a measure of intrinsic viscosity, to be sensitive to CBF. However, previous analysis has shown  $\varphi$  to be highly sensitive to tissue heterogeneities when obtained via algebraic inversion in a way that  $|G^*|$  is not.<sup>55,56</sup> The correlation between  $\varphi$  and CBF was likely lost to noise using the present approach, and analysis methods not limited by homogeneity assumptions may in future reveal significant differences in  $\varphi$  of DGM which elude the present study.<sup>57</sup>

In summary, a correlation of tissue stiffness ( $|G^*|$ ) and average perfusion per vessel size area (flux rate,  $\text{CBF}/A$ ) was observed in deep gray matter when accounting for structurally and functionally distinct areas. In the  $|G^*|$ -CBF space, globus pallidus, hippocampus, thalamus and amygdala clearly cluster from putamen and nucleus accumbens which indicates intrinsic differences in the perfusion pressure gradient. These differences in the microstructural hemodynamic function between the striatum and other deep gray matter regions are not detectable by ASL alone. MR elastography appears to be a promising imaging method for future clinical neuroimaging studies that investigate, for example, the dynamics of stroke<sup>25</sup> or disorders with striatal involvement such as schizophrenia,<sup>58</sup> obesity,<sup>59</sup> or substance addiction.<sup>60</sup>

## Funding

The author(s) disclosed receipt of the following financial support for the research, authorship, and/or publication of this article: IS and JB received funding from the German Research Foundation (grant no. Sa 901/16). Furthermore, IS received funding from the German Federal Ministry of Education and Research (BMBF 01GQ1408) and from the European Union's Horizon 2020 Programme (ID 668039, EU FORCE – Imaging the Force of Cancer).

## Acknowledgements

The authors would like to thank Martin Weygandt, Thomas Christophel and Christian Labadie for the helpful discussions.

## Declaration of conflicting interests

The author(s) declared no potential conflicts of interest with respect to the research, authorship, and/or publication of this article.



### Authors' contributions

SHe and IS conceived and designed the experiments. SHe, PB, AF, Shi, and FD performed the experiments. SHe, IS, and PB were involved in the analysis and interpretation of the data, alongside AF, EB and JB. IS and SHe wrote the manuscript and all authors provided critical revisions.

### References

- Konofagou EE, Harrigan TP, Ophir J, et al. Poroelastography: imaging the poroelastic properties of tissues. *Ultrasound Med Biol* 2001; 27: 1387–1397.
- Leiderman R, Barbone PE, Oberai AA, et al. Coupling between elastic strain and interstitial fluid flow: ramifications for poroelastic imaging. *Phys Med Biol* 2006; 51: 6291–6313.
- Parker KJ. Experimental evaluations of the microchannel flow model. *Phys Med Biol* 2015; 60: 4227–4242.
- Syková E and Nicholson C. Diffusion in brain extracellular space. *Physiol Rev* 2008; 88: 1277–1340.
- Chatelin S, Humbert-Claude M, Garteiser P, et al. Cannabinoid receptor activation in the juvenile rat brain results in rapid biomechanical alterations: Neurovascular mechanism as a putative confounding factor. *J Cereb Blood Flow Metab* 2016; 36: 954–964.
- Hirsch S, Klatt D, Freimann F, et al. In vivo measurement of volumetric strain in the human brain induced by arterial pulsation and harmonic waves. *Magn Reson Med* 2013; 70: 671–683.
- Jugé L, Petiet A, Lambert SA, et al. Microvasculature alters the dispersion properties of shear waves—a multi-frequency MR elastography study. *NMR Biomed* 2015; 28: 1763–1771.
- McGarry MDJ, Johnson CL, Sutton BP, et al. Suitability of poroelastic and viscoelastic mechanical models for high and low frequency MR elastography. *Med Phys* 2015; 42: 947–957.
- Mousavi SR, Fehlner A, Streitberger K-J, et al. Measurement of in vivo cerebral volumetric strain induced by the Valsalva maneuver. *J Biomech* 2014; 47: 1652–1657.
- Perríñez PR, Kennedy FE, Van Houten EEW, et al. Modeling of soft poroelastic tissue in time-harmonic MR elastography. *IEEE Trans Biomed Eng* 2009; 56: 598–608.
- Weaver JB, Pattison AJ, McGarry MD, et al. Brain mechanical property measurement using MRE with intrinsic activation. *Phys Med Biol* 2012; 57: 7275–7287.
- Sener RN. Diffusion MRI: apparent diffusion coefficient (ADC) values in the normal brain and a classification of brain disorders based on ADC values. *Comput Med Imag Graph* 2001; 25: 299–326.
- Wagshul ME, Eide PK and Madsen JR. The pulsating brain: a review of experimental and clinical studies of intracranial pulsatility. *Fluids Barriers CNS* 2011; 8: 5.
- Stoquart-Elsankari S, Lehmann P, Villette A, et al. A phase-contrast MRI study of physiologic cerebral venous flow. *J Cereb Blood Flow Metab* 2009; 29: 1208–1215.
- Le Bihan D. Theoretical principles of perfusion imaging. Application to magnetic resonance imaging. *Invest Radiol* 1992; 27: S6–S11.
- Alsop DC, Detre JA, Golay X, et al. Recommended implementation of arterial spin-labeled perfusion MRI for clinical applications: a consensus of the ISMRM perfusion study group and the European consortium for ASL in dementia. *Magn Reson Med* 2015; 73: 102–116.
- Kaster T, Sack I and Samani A. Measurement of the hyperelastic properties of ex vivo brain tissue slices. *J Biomech* 2011; 44: 1158–1163.
- Chatelin S, Constantinesco A and Willinger R. Fifty years of brain tissue mechanical testing: from in vitro to in vivo investigations. *Biorheology* 2010; 47: 255–276.
- Detre JA, Leigh JS, Williams DS, et al. Perfusion imaging. *Magn Reson Med* 1992; 23: 37–45.
- Muthupillai R, Lomas DJ, Rossman PJ, et al. Magnetic resonance elastography by direct visualization of propagating acoustic strain waves. *Science* 1995; 269: 1854–1857.
- Fehlner A, Behrens JR, Streitberger K-J, et al. Higher-resolution MR elastography reveals early mechanical signatures of neuroinflammation in patients with clinically isolated syndrome. *J Magn Reson Imaging* 2016; 44: 51–58.
- Romano A, Guo J, Prokscha T, Meyer T, et al. In vivo waveguide elastography: effects of neurodegeneration in patients with amyotrophic lateral sclerosis. *Magn Reson Med* 2014; 72: 1755–1761.
- Huston J, Murphy MC, Boeve BF, et al. Magnetic resonance elastography of frontotemporal dementia. *J Magn Reson Imaging* 2016; 43: 474–478.
- Freimann FB, Müller S, Streitberger K-J, et al. MR elastography in a murine stroke model reveals correlation of macroscopic viscoelastic properties of the brain with neuronal density. *NMR Biomed* 2013; 26: 1534–1539.
- Martín A, Macé E, Boisgard R, et al. Imaging of perfusion, angiogenesis, and tissue elasticity after stroke. *J Cereb Blood Flow Metab* 2012; 32: 1496–1507.
- Yin Z, Glaser KJ, Manduca A, et al. Slip interface imaging predicts tumor-brain adhesion in vestibular schwannomas. *Radiology* 2015; 277: 507–517.
- Calamante F, Thomas DL, Pell GS, et al. Measuring cerebral blood flow using magnetic resonance imaging techniques. *J Cereb Blood Flow Metab* 1999; 19: 701–735.
- van Gelderen P, de Zwart JA and Duyn JH. Pitfalls of MRI measurement of white matter perfusion based on arterial spin labeling. *Magn Reson Med* 2008; 59: 788–795.
- Wu W-C, Fernández-Seara M, Detre JA, et al. A theoretical and experimental investigation of the tagging efficiency of pseudocontinuous arterial spin labeling. *Magn Reson Med* 2007; 58: 1020–1027.
- Li X, Wang D, Auerbach EJ, et al. Theoretical and experimental evaluation of multi-band EPI for high-resolution whole brain pCASL imaging. *NeuroImage* 2015; 106: 170–181.
- Wang Z, Aguirre GK, Rao H, et al. Empirical optimization of ASL data analysis using an ASL data processing toolbox: ASLtbx. *Magn Reson Imag* 2008; 26: 261–269.

32. Wang J, Zhang Y, Wolf RL, et al. Amplitude-modulated continuous arterial spin-labeling 3.0-T perfusion MR imaging with a single coil: feasibility study. *Radiology* 2005; 235: 218–228.
33. Shen Y, Pu IM, Ahearn T, et al. Quantification of venous vessel size in human brain in response to hypercapnia and hyperoxia using magnetic resonance imaging. *Magn Reson Med* 2013; 69: 1541–1552.
34. Guo J, Hirsch S, Fehlner A, et al. Towards an elastographic atlas of brain anatomy. *PLoS One* 2013; 8: e71807.
35. Streitberger K-J, Reiss-Zimmermann M, Freimann FB, et al. High-resolution mechanical imaging of glioblastoma by multifrequency magnetic resonance elastography. *PLoS One* 2014; 9: e110588.
36. Hirsch S, Braun J and Sack I. *Magnetic resonance elastography: Physical background and medical applications*. Weinheim, Germany: Wiley-VCH Verlag GmbH & Co. KGaA, 2017.
37. Hirsch S, Guo J, Reiter R, et al. MR elastography of the liver and the spleen using a piezoelectric driver, single-shot wave-field acquisition, and multifrequency dual parameter reconstruction. *Magn Reson Med* 2014; 71: 267–277.
38. Braun J, Guo J, Lützkendorf R, et al. High-resolution mechanical imaging of the human brain by three-dimensional multifrequency magnetic resonance elastography at 7T. *NeuroImage* 2014; 90: 308–314.
39. Fehlner A, Papazoglou S, McGarry MD, et al. Cerebral multifrequency MR elastography by remote excitation of intracranial shear waves. *NMR Biomed* 2015; 28: 1426–1432.
40. Fehlner A, Hirsch S, Weygandt M, et al. Increasing the spatial resolution and sensitivity of magnetic resonance elastography by correcting for subject motion and susceptibility-induced image distortions. *J Magn Reson Imaging*. Epub ahead of print 20 October 2016; DOI: 10.1002/jmri.25516.
41. Tzourio-Mazoyer N, Landeau B, Papathanassiou D, et al. Automated anatomical labeling of activations in SPM using a macroscopic anatomical parcellation of the MNI MRI single-subject brain. *NeuroImage* 2002; 15: 273–289.
42. Murphy MC, Huston J, Jack CR, et al. Measuring the characteristic topography of brain stiffness with magnetic resonance elastography. *PLoS One* 2013; 8: e81668.
43. Holm S. A simple sequentially rejective multiple test procedure. *Scand J Stat* 1979; 6: 65–70.
44. Rousseeuw PJ. Silhouettes: a graphical aid to the interpretation and validation of cluster analysis. *J Comput Appl Math* 1987; 20: 53–65.
45. Fan AP, Jahanian H, Holdsworth SJ, et al. Comparison of cerebral blood flow measurement with [15O]-water positron emission tomography and arterial spin labeling magnetic resonance imaging: A systematic review. *J Cereb Blood Flow Metab* 2016; 36: 842–861.
46. Telischak NA, Detre JA and Zaharchuk G. Arterial spin labeling MRI: clinical applications in the brain. *J Magn Reson Imaging* 2015; 41: 1165–1180.
47. Dittmann F, Tzschätzsch H, Hirsch S, et al. Tomoelastography of the abdomen: Tissue mechanical properties of the liver, spleen, kidney, and pancreas from single MR elastography scans at different hydration states. *Magn Reson Med*. Epub ahead of print 3 October 2016; DOI: 10.1002/mrm.26484.
48. Nieuwenhuys R, Voogd J and Huijzen C. *The human central nervous system: a synopsis and atlas*. Berlin: Springer Science & Business Media, 2013.
49. Carhuapoma JR, Mayer SA and Hanley DF. *Intracerebral hemorrhage*, 1st ed. New York: Cambridge University Press, 2009.
50. Paciaroni M, Agnelli G, Caso V, et al. *Manifestations of stroke*. New York: Karger Medical and Scientific Publishers, 2012.
51. Gould IG, Tsai P, Kleinfeld D, et al. The capillary bed offers the largest hemodynamic resistance to the cortical blood supply. *J Cereb Blood Flow Metab* 2016; 37: 52–68.
52. Jensen JH, Lu H and Inglese M. Microvessel density estimation in the human brain by means of dynamic contrast-enhanced echo-planar imaging. *Magn Reson Med* 2006; 56: 1145–1150.
53. Arani A, Murphy MC, Glaser KJ, et al. Measuring the effects of aging and sex on regional brain stiffness with MR elastography in healthy older adults. *NeuroImage* 2015; 111: 59–64.
54. Sack I, Beierbach B, Hamhaber U, et al. Non-invasive measurement of brain viscoelasticity using magnetic resonance elastography. *NMR Biomed* 2008; 21: 265–271.
55. Dittmann F, Hirsch S, Tzschätzsch H, et al. In vivo wide-band multifrequency MR elastography of the human brain and liver. *Magn Reson Med* 2015; 76: 1116–1126.
56. Barnhill E, Hollis L, Sack I, et al. Nonlinear multiscale regularisation in MR elastography: Towards fine feature mapping. *Med Image Anal* 2017; 35: 133–145.
57. Johnson CL, Schwarb H, D J McGarry M, et al. Viscoelasticity of subcortical gray matter structures. *Hum Brain Mapp* 2016; 37: 4221–4233.
58. Howes OD and Kapur S. The dopamine hypothesis of schizophrenia: version III—the final common pathway. *Schizophr Bull* 2009; 35: 549–562.
59. Weygandt M, Mai K, Dommes E, et al. The role of neural impulse control mechanisms for dietary success in obesity. *NeuroImage* 2013; 83: 669–678.
60. Heinz A, Siessmeier T, Wrase J, et al. Correlation between dopamine D(2) receptors in the ventral striatum and central processing of alcohol cues and craving. *Am J Psychiatr* 2004; 161: 1783–1789.
61. Buxton RB. Quantifying CBF with arterial spin labeling. *J Magn Reson Imaging* 2005; 22: 723–726.
62. Herscovitch P and Raichle ME. What is the correct value for the brain–blood partition coefficient for water? *J Cereb Blood Flow Metab* 1985; 5: 65–69.
63. Mann DM, Eaves NR, Marcyniuk B, et al. Quantitative changes in cerebral cortical microvasculature in ageing and dementia. *Neurobiol Aging* 1986; 7: 321–330.